Longitudinal and transverse flow over a cavity containing a second immiscible fluid

Clarissa Schönecker† and Steffen Hardt

Institute for Nano- and Microfluidics, Center of Smart Interfaces, Technische Universität Darmstadt, 64287 Darmstadt, Germany

An analytical solution for the low-Reynolds-number flow field of a shear flow over a rectangular cavity containing a second immiscible fluid is derived. While flow of a single-phase fluid over a cavity is a standard case investigated in fluid dynamics, flow over a cavity that is filled with a second immiscible fluid has received little attention. The flow field inside the cavity is considered to define a boundary condition for the outer flow, which takes the form of a Navier slip condition with locally varying slip length. The slip-length function is determined heuristically from the related problem of lid-driven cavity flow. Based on the Stokes equations and complex analysis, it is then possible to derive a closed analytical expression for the flow field over the cavity for both the transverse and the longitudinal case. The result is a comparatively simple function, which displays the dependence of the flow field on the cavity geometry and the medium filling the cavity. The analytically computed expression agrees well with results obtained from a numerical solution of the Navier–Stokes equations.

Key words: interfacial flows (free surface), low-Reynolds-number flows, microfluidics

1. Introduction

Flows in and over cavities are important blueprints for many phenomena in fluid dynamics. On a reduced scale, they illustrate phenomena occurring in various, often more complex, applications. These might, for example, be in aerodynamics, where the vortices forming inside cavities or grooves in surfaces are studied (Moffatt 1963; Pan & Acrivos 1967; Higdon 1985; Shankar & Deshpande 2000). The corresponding flow patterns affect the drag to which a fluid streaming over the surface is subjected (Shen & Floryan 1985; Prasad & Koseff 1989). Traditionally, such troughs, or more generally surface roughness features, have always been perceived as unwanted, since the vortices forming inside the cavities may lead to higher drag or acoustic disturbances. Yet, at higher Reynolds numbers, riblets may also reduce drag, which has been of great interest more recently (Viswanath 2002; Jovanović, Frohnapfel & Delgado 2010).

In all these investigations, only a single fluid phase flowing over the cavity and filling it at the same time is considered. However, there exist numerous applications where a fluid flows over a cavity filled with a second immiscible fluid. It is well known that by capillary condensation vapour condenses in sufficiently small capillaries

† Email address for correspondence: schoenecker@csi.tu-darmstadt.de

or channels although the vapour pressure is below the bulk saturation pressure (Fisher & Israelachvili 1979; Fisher, Gamble & Middlehurst 1981; Ciccotti *et al.* 2008). So does vapour inside the roughness features of a surface. This may have an immediate impact on the applications in aerodynamics mentioned above, since the condensed water has a viscosity different from that of the gas and hence moves at a slower speed. Moreover, we can also encounter the inverse situation, where small bubbles, often of nanometre size, are enclosed in the roughness features of the wall of a water-filled channel (Yang *et al.* 2007). Additionally, all superhydrophobic, lotus leaf-mimicking surfaces take advantage of such enclosed gas (Ma & Hill 2006; Lee, Choi & Kim 2008; Nosonovsky & Bhushan 2008; Rothstein 2010). Other examples are the flow over membranes or porous media, which may be filled with a second immiscible fluid as well.

Besides the work on flows over cavities, which includes the fluid motion inside the cavity, there have also been investigations of flows over surfaces with periodically patterned boundary conditions. In such a context, a cavity is usually represented by a certain boundary condition to the flow above it. The flow inside is not considered. Philip (1972) analyses the flow over a no-shear slot within a no-slip wall in longitudinal and transverse directions. A no-shear interface is certainly the ideal limit, which is approached when the viscosity ratio between the fluid above and inside the cavity tends to infinity, but which cannot be reached by a real viscous fluid. Although this condition is often used for modelling air–liquid interfaces (Lauga & Stone 2003; Sbragaglia & Prosperetti 2007; Davis & Lauga 2009; Crowdy 2010; Davis & Lauga 2010), it is not immediately clear how well air fulfils these ideal characteristics.

The no-shear condition corresponds to an infinite slip length β in the Navier boundary condition (Navier 1823)

$$u|_{boundary} = \beta \left.\frac{\partial u}{\partial y}\right|_{boundary},$$
(1.1)

which allows for a non-zero velocity u at the boundary. The slip length β relates the velocity to its gradient in the direction normal to the surface $\partial u/\partial y$ and can be understood as an imaginary depth below the surface at which the velocity extrapolates to zero. It has become a standard boundary condition for describing slip, being used in a variety of calculations (e.g. Cottin-Bizonne *et al.* 2004; Ybert *et al.* 2007). Still, when employing (1.1) for the modelling of a fluid-filled cavity, it is by no means clear how to specifically choose β. Belyaev & Vinogradova (2010) have calculated a flow over an array of slots with constant slip length. However, it remains unclear how β is related to the slot geometry or to the properties of the fluid filling the cavities. Furthermore, in reality, the slip length will not be constant but will be a spatially varying quantity. So far, Hocking (1976) has briefly addressed the effect of the viscosity of the medium inside a cavity, but only found an approximation to the streamlines in terms of an infinite Fourier series in the case of an infinite slip length.

In this paper, a representation of a rectangular cavity in the form of a boundary condition for a second immiscible fluid flowing over a surface is described. It is directly related to the flow pattern inside the cavity, i.e. to the geometry of the cavity and the viscosity of the fluid it contains. The effect of these properties on the outer flow can therefore be directly explored.

Based on this, we calculate the flow field of a shear flow directed transversely and longitudinally with respect to the cavity. The solution to this mixed boundary value
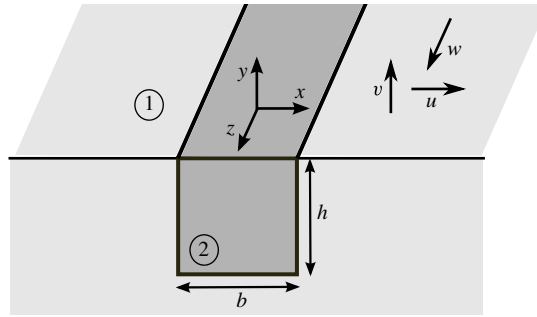
FIGURE 1. Schematic of the considered cavity with coordinate and velocity directions.

problem can be obtained through a representation of the flow by complex variables. Unlike with the often employed methods based on Fourier series, we can derive a closed-form expression and present a simple explicit formula for the flow field.

2. Model of the cavity and boundary conditions

We consider a rectangular cavity of depth h, width b and infinite extension in the z direction as depicted in figure 1. Fluid 1 flows over the cavity, while fluid 2 fills the same. The interface between the two fluids is assumed to be flat. For small cavities, this is usually justified, since surface tension provokes a flattening of the interface and will only permit negligibly small curvatures (Higdon 1985). In more general terms, it means that we consider a flow problem at sufficiently small capillary numbers. Additionally, we do not allow for a pressure gradient to be applied across the interface, as is sometimes done (Biben & Joly 2008; Tsai *et al.* 2009), leading to a modification of the shear stress (Steinberger *et al.* 2007). By considering the basic case of a flat interface, we ensure that an analytic solution is possible.

In the following, a boundary condition is derived, describing the effect of the cavity on the outer flow. It can be employed without the need to calculate the detailed flow inside the cavity.

2.1. *General form of the boundary conditions and the role of viscosity*

A first-principles modelling of the cavity is achieved by taking into account the viscosity of the medium inside the cavity and the geometry of the cavity. The mathematical framework is exemplified for a flow perpendicular to the cavity. The longitudinal case is analogous.

At the fluid–fluid interface, continuity of velocity and shear stress applies, i.e.

$$\left. \begin{array}{r} u_1 = u_2 \\[4pt] \eta_1 \dfrac{\partial u_1}{\partial y} = \eta_2 \dfrac{\partial u_2}{\partial y} \end{array} \right\} \quad \text{for } |x| < \frac{b}{2}, \quad y = 0, \tag{2.1}$$

while at the wall, the no-slip condition

$$u_1 = 0 \quad \text{for } |x| > \frac{b}{2}, \quad y = 0 \tag{2.2}$$

holds, where u denotes the velocity in the x direction and η is the dynamic viscosity. The indices 1 and 2 refer to the respective fluids.

The boundary conditions (2.1) and (2.2) are valid for problems at a scale large enough to neglect discontinuities of the velocity at the fluid–fluid and solid–fluid interfaces. In that context, a distinction has to be made between liquid and gas flows. For gas flows, the velocity discontinuities, expressed in terms of a slip length, can be quite large. Depending on the type of reflection boundary condition for the gas molecules (rather diffuse or rather specular), the slip length is of the order of the molecular mean free path or even larger (Karniadakis, Beskok & Aluru 2005). For liquid flows along solid surfaces, the problem of boundary slip has been studied quite extensively. For simple liquids, significant values of the slip length of the order of 10 nm are preferentially found on hydrophobic surfaces (for an overview, see Lauga, Brenner & Stone 2005). The problem of slip along liquid–liquid interfaces has been studied to a much lesser extent. Results from molecular dynamics simulations indicate that, for that case, the slip length is very small, of the order of a few molecular diameters (Galliero 2010; Hu, Zhang & Wang 2010). Relating the problem investigated in this paper to these findings, in each case it has to be ensured that the length scale characterizing the cavity is much larger than the slip length for the case under study. Nevertheless, the mathematical method outlined in the course of this paper can also be employed to compute the flow in cases where a velocity jump occurs at the wall or at the fluid–fluid interface.

The velocity u_2 at the upper side of the cavity can be written as a Navier slip condition

$$u_2(x, 0) = \gamma(x) \left.\frac{\partial u_2}{\partial y}\right|_{y=0}, \qquad (2.3)$$

with the local slip-length function $\gamma(x)$ to be determined. Incorporating this equation, the two transition conditions (2.1) collapse into one boundary condition, such that the boundary conditions for fluid 1 are

$$u_1 = N\gamma(x)\frac{\partial u_1}{\partial y} \quad \text{for } |x| < \frac{b}{2}, \quad y = 0, \qquad (2.4)$$

$$u_1 = 0 \quad \text{for } |x| > \frac{b}{2}, \quad y = 0, \qquad (2.5)$$

with N abbreviating the viscosity ratio of the two fluids, i.e.

$$N = \frac{\eta_1}{\eta_2}. \qquad (2.6)$$

Equation (2.4) again has the form of a Navier slip condition with a net slip length for fluid 1 being the product of the viscosity ratio and the slip-length function.

At low Reynolds numbers, the flow pattern inside the cavity can be assumed to be independent of the viscosity ratio. Hence, the local slip-length distribution $\gamma(x)$ solely stems from the geometry of the cavity. The effects of N and $\gamma(x)$ on the outer flow field are therefore decoupled. While N always enters the net slip length linearly, the slip-length function involves the principal part of the modelling.

As soon as the slip-length function has been determined, the flow over the cavity can be studied without the need to compute the flow field inside the cavity. This is of great advantage for analytical calculations. Since, in the following, the focus is on the flow over the surface outside of the cavity, the subscript 1 is no longer needed and is dropped from now on.

A	0.25	0.50	1.0	2.0	5.0
d^*/b	0.0875	0.1628	0.24	0.25	0.25

TABLE 1. Centre of the first vortex; after Pan & Acrivos (1967).

2.2. *Modelling of the local slip-length function and the role of the cavity geometry*

The local slip-length distribution is determined by the geometry of the cavity. Here we consider a rectangular cavity, characterized by its depth h and width b, but a similar procedure can also be imagined for a differently shaped cavity.

Basically, we look for a differentiable function $\gamma(x)$. At the corners $x = \pm b/2$, obviously $\gamma(x) = 0$ to make the two boundary conditions match, i.e. for the flow velocity to be continuous. At the centre of the cavity at $x = 0$, the flow is least suppressed by the walls of the cavity, and hence the slip length reaches a maximum d.

A universal description of the local slip-length function could only be obtained as an infinite series of eigenfunctions. Therefore, we introduce a heuristic step to incorporate the influence of the cavity geometry in a simple manner.

Requiring $\gamma(\pm b/2) = 0$ and $\gamma(0) = d$, as a first step, we assume $\gamma(x)$ to be of elliptic form with semi-axes d and $b/2$. This particular choice allows a closed-form solution to be calculated for the flow field, as will become clear in the following section. In addition, for a wide range of aspect ratios A, it already gives remarkably good results. It is possible to modify the specific form subsequently. The modelling of the maximum of the local slip length d is inspired by the investigation of lid-driven cavity flows. Here, the upper boundary of the cavity is also considered to be flat.

In lid-driven cavities, one or more counter-rotating vortices of decreasing intensity develop. The greater the aspect ratio $A = h/b$ of the cavity, i.e. the deeper the cavity, the more vortices are created (Pan & Acrivos 1967; Joseph & Sturges 1978; Higdon 1985; Shankar 1993; Shankar & Deshpande 2000). An important parameter addressed in those investigations has always been the location of the vortex centres. For low Reynolds numbers, the centres of these vortices are always located on the centreline of the cavity $x = 0$. The distance from the centre of the first of these vortices to the top of the cavity d^* should give an upper bound to d. This is due to the shape of the velocity field (cf. Higdon 1985) being driven by the upper boundary.

Pan & Acrivos (1967) give the centre of the first vortex d^*/b as a function of the aspect ratio (see table 1). From these results, we can distinguish two regimes. At low aspect ratios, the position of the first vortex develops nearly linearly with A. The characteristic length is the cavity depth h. Around an aspect ratio of $A = 1$, a plateau is reached, so that at high aspect ratios, the position of the first vortex is constant and the characteristic length is the cavity width b. Such a behaviour, a nearly linear dependence suddenly followed by a plateau, is quite generally encountered in a variety of physical problems, for example, in the diffusion of mass or heat when one boundary is subject to a sudden change. The solution of these problems is often described by an error function. Indeed, an ansatz of the form $d^*/b = c_0 + \mathrm{erf}(c_1 A)$ fits well the data given by Pan & Acrivos (1967) with the constants $c_0 \approx 0.251$ and $c_1 \approx 1.319$.

This relation describes the order of magnitude of the maximum local slip length d, since the vortex centre d^* should be an upper bound to d. It already captures the essential parametric dependences of the slip-length function; however, a more exact description can be obtained. As we consider the linear flow regime at small Reynolds

numbers, we expect a similar behaviour for d as for d^*. We choose the ansatz

$$D = d/b = d_0 \cdot \mathrm{erf}(d_1 A) \tag{2.7}$$

with two constants d_0 and d_1. They can be determined by examination of the two limiting cases of small and large A.

For very shallow cavities, there is only one vortex present in the cavity. In the limit of $A \to 0$, the flow of fluid 2 corresponds to a thin-film flow and is governed by the lubrication approximation of the Navier–Stokes equations

$$\frac{\partial p_2}{\partial x} = \eta_2 \frac{\partial^2 u_2}{\partial y^2}, \tag{2.8}$$

$$\frac{\partial p_2}{\partial y} = 0. \tag{2.9}$$

The solution for u_2 is readily integrated to be a polynomial of second order. The boundary conditions

$$u_2|_{y=0} = d \left.\frac{\partial u_2}{\partial y}\right|_{y=0}, \quad u_2|_{y=-h} = 0, \tag{2.10}$$

and mass conservation

$$\int_{y=-h}^{y=0} u_2 = 0 \tag{2.11}$$

yield the size of the slip length

$$D = \tfrac{1}{4} A. \tag{2.12}$$

In the limit of $A \to 0$, D thus depends on the aspect ratio with a slope of $1/4$, i.e.

$$\lim_{A \to 0} \frac{\mathrm{d}D}{\mathrm{d}A} = \frac{1}{4}, \tag{2.13}$$

which is less than the corresponding slope of the vortex centre and thus consistent.

The height of the plateau of D at large A is limited by c_0; however, its accurate value has to be determined numerically. Assuming that the plateau is reached at $A = 10$ and that the mean values of the local slip length on the cavity match in the analytical and numerical cases, a simulation of water flowing over an air-filled cavity of $A = 10$, which will be described in more detail later, leads to the condition

$$\lim_{A \to \infty} D = 0.124. \tag{2.14}$$

Hence, the maximum of the elliptic slip-length distribution for transverse flow can be described by

$$D_t = d_{0,t} \cdot \mathrm{erf}\left(\frac{\sqrt{\pi}}{8 d_{0,t}} A\right) \tag{2.15}$$

with $d_{0,t} = 0.124$.

For longitudinal flow, when the second fluid can enter and leave the cavity, there is no backflow and a corresponding calculation leads to

$$D_l = d_{0,l} \cdot \mathrm{erf}\left(\frac{\sqrt{\pi}}{2 d_{0,l}} A\right) \tag{2.16}$$

with $d_{0,l} = 0.347$.

This rather heuristic approach for determining $\gamma(x)$ can be formalized by introducing iterative maps

$$\Gamma_1 : U_i(x) \to \gamma_i(x) \tag{2.17}$$

and

$$\Gamma_2 : \gamma_i(x) \to U_{i+1}(x). \tag{2.18}$$

Here Γ_1 denotes that, from the solution of the generalized lid-driven cavity problem with a velocity distribution $U_i(x)$ prescribed at the upper boundary of the cavity, a slip-length function $\gamma_i(x)$ is determined. And Γ_2 maps a slip-length function used as a boundary condition at the top of the cavity to the velocity distribution at this boundary. Successive application of the map $\Gamma_1 \circ \Gamma_2$ generates a series of approximations $\gamma_i(x)$ ($i = 1, 2, \ldots$) to the slip-length function $\gamma(x)$, i.e. $\lim_{i \to \infty} \gamma_i(x) = \gamma(x)$, provided that the iteration scheme converges. Below we will show that, when starting with $U_1(x) = \mathrm{const.}$, already $\gamma_1(x)$ – determined in a simplified manner – yields a good approximation to the flow field above the cavity. Therefore, in the framework of this paper, no further iterations will be performed.

3. Transverse flow

In the following, a fluid flow in the x direction over the cavity is investigated and its flow field is derived. The fluid is driven by a constant shear stress τ_∞ in the x direction at $y \to \infty$.

At sufficiently small Reynolds numbers, the flow obeys the Stokes equations

$$-\frac{\partial p}{\partial x} + \eta_1 \left(\frac{\partial^2 u}{\partial x^2} + \frac{\partial^2 u}{\partial y^2} \right) = 0, \tag{3.1}$$

$$-\frac{\partial p}{\partial y} + \eta_1 \left(\frac{\partial^2 v}{\partial x^2} + \frac{\partial^2 v}{\partial y^2} \right) = 0, \tag{3.2}$$

where u and v are the velocities in the x and y directions, respectively, and p is the pressure. With the stream function

$$\frac{\partial \Psi}{\partial x} = -v \quad \text{and} \quad \frac{\partial \Psi}{\partial y} = u, \tag{3.3}$$

the Stokes equations transform into the biharmonic equation

$$\Delta \Delta \Psi = 0. \tag{3.4}$$

The solution to the biharmonic equation is given by Goursat's theorem (Smirnow 1974; Muskhelishvili 1975), a special form of which reads

$$\Psi = \mathrm{Re}\left((\bar{\mathfrak{z}} - \mathfrak{z}) W_t(\mathfrak{z}) \right). \tag{3.5}$$

The Goursat function $W_t(\mathfrak{z})$ is an analytic function to be found, with the subscript t indicating the transverse flow direction. Re is the real part and the complex coordinate is given by

$$\mathfrak{z} = x + \mathrm{i}y \quad \text{and} \quad \bar{\mathfrak{z}} = x - \mathrm{i}y. \tag{3.6}$$

In (3.5), the general Goursat theorem containing two Goursat functions has been reduced to an expression containing only one unknown function by elimination of the undetermined constant in the stream function. Owing to the impermeability of
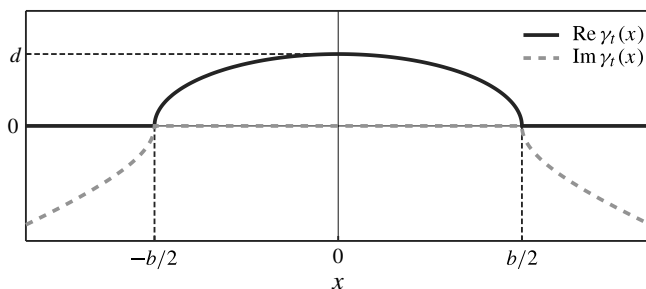
FIGURE 2. Real (solid line) and imaginary (dashed line) part of $\gamma_t(x)$.

walls lying on the real axis, the stream function is set to zero at these boundaries (cf. Garabedian 1966; Philip 1972). Expression (3.5) has been used previously in the solution of similar problems (Atanacković 1977; Philip 1972).

With the ansatz (3.5) the boundary conditions (2.4) and (2.5) read

$$\text{Im}(W_t) = 2N\gamma_t(x)\,\text{Re}(W_t') \quad \text{for } |x| < \frac{b}{2}, \quad y = 0, \tag{3.7}$$

$$\text{Im}(W_t) = 0 \quad \text{for } |x| > \frac{b}{2}, \quad y = 0. \tag{3.8}$$

The prime denotes the derivative with respect to $\mathfrak{z}$.

As an elementary mathematical case, the slip-length function $\gamma_t(x)$ is assumed to be of elliptic form, fulfilling the conditions of § 2. In complex notation $\gamma_t(x)$ can be written as

$$\gamma_t(x) = -\mathrm{i}2D_t\sqrt{x^2 - \frac{b^2}{4}}, \tag{3.9}$$

which is real for $|x| < b/2$ and imaginary for $|x| > b/2$ (figure 2). This form is essential for keeping the following calculations analytically tractable. Nevertheless, one is not restricted to an ellipse. Cherepanov (1977, pp. 68–69) outlined a method of approximating any arbitrary function that is continuous on a finite interval and vanishes at its ends as a complex function, whose value is real on the interval and imaginary outside the interval. This method provides a general framework for investigation of flow over differently shaped cavities, e.g. triangular or rounded ones, provided that the local slip-length function is known for the cavity of interest. However, for convenience we will use the expression of (3.9).

Similarly to the boundary conditions at $y = 0$, the condition of a given shear stress $\tau_\infty = \eta_1\,\partial u/\partial y$ at infinity can be written in terms of $W_t(\mathfrak{z})$ as

$$\text{Re}(W_t') = \frac{\tau_\infty}{4\eta_1} \quad \text{for } y \to \infty. \tag{3.10}$$

The solution procedure follows the method of Sotkilava & Cherepanov (1974), originally employed in elasticity theory. An auxiliary function

$$F_t(\mathfrak{z}) = W_t'(\mathfrak{z}) - \frac{1}{4D_tN\sqrt{\mathfrak{z}^2 - \frac{1}{4}b^2}}W_t(\mathfrak{z}) \tag{3.11}$$

is chosen such that the boundary conditions (3.7) and (3.8) take the form

$$\mathrm{Re}(F_t(\mathfrak{z})) = 0 \quad \text{for } |x| < \frac{b}{2}, \quad y = 0, \tag{3.12}$$

$$\mathrm{Im}(F_t(\mathfrak{z})) = 0 \quad \text{for } |x| > \frac{b}{2}, \quad y = 0. \tag{3.13}$$

The condition at infinity (3.10) is

$$\mathrm{Re}(F_t(\mathfrak{z})) = \frac{\tau_\infty}{4\,\eta_1} \left(1 - \frac{1}{4D_t N} \right) \quad \text{for } y \to \infty. \tag{3.14}$$

The conditions (3.12) and (3.13) constitute a mixed boundary value problem for the half-plane. Its solution is given by the Keldysh–Sedov formula (Keldysh & Sedov 1937; Muskhelishvili 2008). Since (3.12) and (3.13) are homogeneous, only the homogeneous part of the Keldysh–Sedov formula is required, which reads

$$F_t(\mathfrak{z}) = \frac{L(\mathfrak{z})}{\sqrt{\mathfrak{z}^2 - \frac{1}{4}b^2}}. \tag{3.15}$$

In our case, $L(\mathfrak{z})$ is a linear function with two real coefficients (Lawrentjew & Schabat 1967) to be determined. This is achieved by requiring the condition at infinity (3.14), giving

$$F_t(\mathfrak{z}) = \frac{\tau_\infty}{4\eta_1} \left(1 - \frac{1}{4D_t N} \right) \frac{\mathfrak{z}}{\sqrt{\mathfrak{z}^2 - \frac{1}{4}b^2}}. \tag{3.16}$$

The auxiliary differential equation (3.11) can now be solved. Its general solution is

$$W_t(\mathfrak{z}) = W_0(\mathfrak{z}) \left(C + \int_{\mathfrak{z}0}^{\mathfrak{z}} F_t(\mathfrak{Z}) W_0^{-1}(\mathfrak{Z}) \, \mathrm{d}\mathfrak{Z} \right), \tag{3.17}$$

with the solution to the homogeneous problem

$$W_0(\mathfrak{z}) = \exp \left(\int_{\mathfrak{z}0}^{\mathfrak{z}} \frac{1}{4D_t N \sqrt{\mathfrak{Z}^2 - \frac{1}{4}b^2}} \, \mathrm{d}\mathfrak{Z} \right) \tag{3.18}$$

and the constant C to be determined from the condition of symmetry, i.e.

$$\mathrm{Im}(W_t'(\mathfrak{z})) = 0 \quad \text{at } \mathfrak{z} = 0, \tag{3.19}$$

ensuring the analyticity of $W_t(\mathfrak{z})$.

Integrating from $\mathfrak{z}0 = b/2$, i.e. evaluating the Cauchy principal value of the integrals in (3.17) and (3.18), the result for $W_t(\mathfrak{z})$ is computed as

$$W_t(\mathfrak{z}) = \frac{\tau_\infty}{4\eta_1} \frac{\mathfrak{z} + 4D_t N \sqrt{\mathfrak{z}^2 - \frac{1}{4}b^2}}{1 + 4D_t N}. \tag{3.20}$$

Following Goursat's theorem (3.5), the expression for the stream function is

$$\Psi = \frac{\tau_\infty}{2\eta_1} \frac{y}{1 + 4D_t N} \left(y + 4D_t N \mathrm{Im} \sqrt{(x + \mathrm{i}y)^2 - \frac{1}{4}b^2} \right). \quad (3.21)$$

This result is consistent with the work of Philip (1972), who calculated the transverse flow over a no-shear slot. In the limit of a very low-viscosity fluid in the cavity, we obtain

$$\lim_{N \to \infty} \Psi = \frac{\tau_\infty}{2\eta_1} y \, \mathrm{Im} \sqrt{(x + \mathrm{i}y)^2 - \frac{1}{4}b^2}, \quad (3.22)$$

which is equivalent to Philip's result.

When evaluating (3.21) in the second quadrant of $\mathfrak{z}$, one should be aware of crossing a branch cut, which for a square root is usually chosen along the negative real axis. To avoid ambiguity, one may wish to write $\mathrm{i}\sqrt{b^2/4 - \mathfrak{z}^2}$ instead of $\sqrt{\mathfrak{z}^2 - b^2/4}$ for $x < 0$.

In figure 3, the streamlines are plotted in the form

$$\tilde{\Psi} = \Psi \frac{8\eta_1}{\tau_\infty b^2} = \frac{Y}{1 + 4D_t N} \left(Y + 4D_t N \, \mathrm{Im} \sqrt{(X + \mathrm{i}Y)^2 - 1} \right), \quad (3.23)$$

with $X = x(2/b)$ and $Y = y(2/b)$. The only flow-determining parameters are D_t, the ratio of the maximum local slip length and the cavity width, and the viscosity ratio N. Figure 3 shows the streamlines for cavities that are deeper than they are wide ($D_t = 0.124$) and varying N. Clearly, the higher the viscosity ratio, i.e. the lower the viscosity of the cavity medium, the more the presence of the cavity influences the flow over the wall. For a high viscosity ratio, the flow is notably accelerated towards the cavity; while for a small viscosity ratio, the flow pattern approaches that of a plain wall.

This behaviour is explicitly apparent from figure 4. The velocity u at the boundary $y = 0$ is normalized with $u_{p,max}$, being the maximum achievable velocity for the perfect slip case $N \to \infty$ at $x = y = 0$. The velocity obviously increases with N. In the same manner, for low N the shear stress at $y = 0$ is similar to the average shear stress, while being reduced towards zero for high N.

It can be further observed that, for the chosen elliptic slip-length distribution $\gamma_t(x)$, the shear stress is constant along the cavity. A similar relationship exists in elasticity theory, when a flat, rigid stamp, pressed into an elastic material, provokes an elliptic pressure distribution underneath the stamp (Muskhelishvili 1975). The constant shear stress also follows from (3.20). At $y = 0$ and $|x| < (b/2)$, the shear stress is

$$\eta_1 \frac{\partial u}{\partial y} = 4\eta_1 \, \mathrm{Re}(W_t') = \frac{\tau_\infty}{1 + 4D_t N} = \mathrm{const.} \quad (3.24)$$

Hence, (3.23) not only describes shear flow over an elliptic slip-length distribution, but also is a general solution of the biharmonic equation with mixed no-slip and constant-shear boundary conditions, similar to Philip's result for mixed no-slip and no-shear conditions.

It should be noted that for $N = 1$ the flow field is not identical to the case of a single-phase flow. The flow profile is modified due to the flat fluid–fluid interface, which strictly separates both fluids and cannot be crossed.

In the case of water flowing over an air-containing cavity, the maximum velocity at $x = 0$ is $u_0/u_{p,max} = 0.965$ and the shear stress is $\tau/\tau_\infty = 0.035$ for cavities that
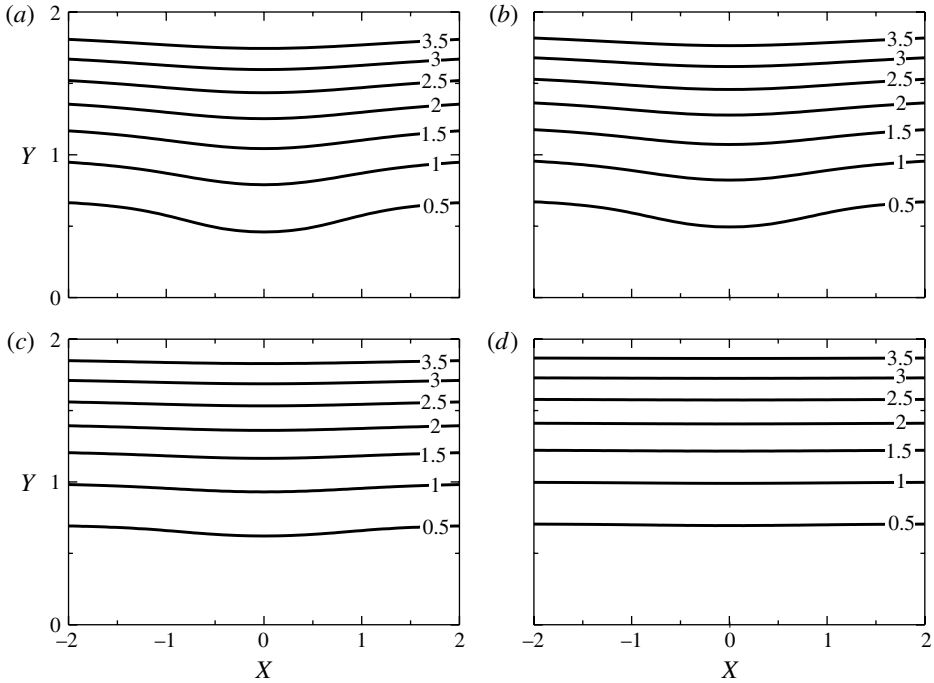
FIGURE 3. Transverse flow streamline patterns $\tilde{\Psi}$ for $D_t = 0.124$ and varying viscosity ratio: (*a*) $N = 100$; (*b*) $N = 10$; (*c*) $N = 1$; (*d*) $N = 0.1$.
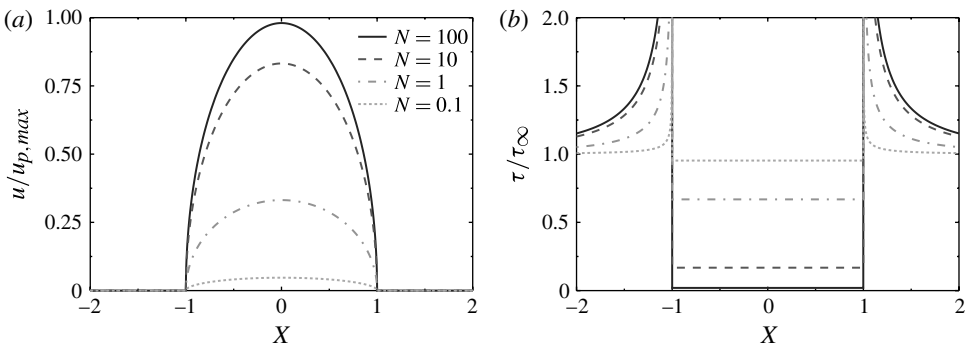

FIGURE 4. Normalized (*a*) velocity and (*b*) shear stress along the boundary $y = 0$.

are deeper than they are wide ($D_t = 0.124$). These numbers illustrate the accuracy of previous models, where a vanishing shear stress is assumed at the air–water interface. For cavities that are deeper than they are wide, the maximum velocity was hence calculated $\sim 3.5\%$ too high.

For lower viscosity ratios than for the water–air system ($N \approx 56$), the influence of the cavity depth becomes more prominent, which can be observed from figure 5. Here, the dependence of the normalized velocity $u_0/u_{p,max}$ at $\mathfrak{z} = 0$ on the aspect ratio of the cavity A is shown for various values of N. It can be observed that the influence of a variation of N on $u_0/u_{p,max}$, translating to a modification of the outer flow field, is strongest around $N = 1$. At very large or small values of N, a variation of N has only
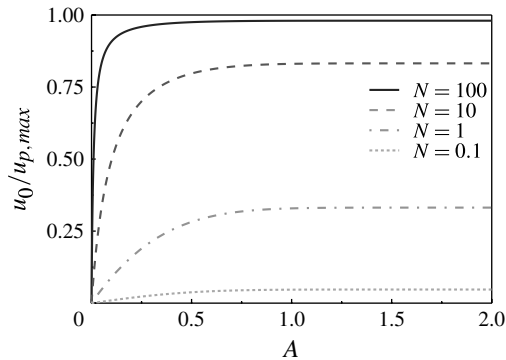
FIGURE 5. Variation of the velocity at $\mathfrak{z} = 0$ with the aspect ratio of the cavity A for a range of viscosity ratios N.

a small effect. This fact is also apparent in figures 3(*a*) and 3(*b*), which differ only slightly.

As explained above, $\gamma(x)$ may be a general function, with $\gamma(\pm b/2) = 0$ and a maximum $\gamma(0) = d$. As a minimum model and in order to keep the calculations analytically tractable, we have employed an elliptic form, with d being described by a heuristic equation inspired by lid-driven cavity flows. In order to assess the accuracy of this model, its results are compared to numerical calculations.

Both the fluid inside the cavity as well as the fluid flowing over the cavity are included in the numerical calculation. As a typical example, water (density $\rho = 10^3$ kg m^{-3} and dynamic viscosity $\eta = 10^{-3}$ Pa s) and air ($\rho = 1.2$ kg m^{-3}, $\eta = 1.8 \times 10^{-5}$ Pa s) have been considered. At the interface between the fluids, continuity of velocity and stress (2.1) holds. The dimensions of the cavity are $b = h = 50$ µm. At a distance to the wall of $y = 500$ µm, a shear stress of 0.1 Pa is imposed, so that $Re = u|_{x=0,y=0} \, b\rho/\eta \ll 1$ for both fluids. It should be noted that at this point the dimensions of the cavity have only been specified as typical examples. In the low-Reynolds-number limit, the results for a rescaled cavity are identical. The Navier–Stokes equations have been solved with the commercial finite-element software COMSOL Multiphysics (COMSOL Multiphysics GmbH, Göttingen) in a computational domain of 3 mm width with a triangular mesh of approximately 65 000 elements. The mesh was strongly refined along the fluid–fluid interface to accommodate the discontinuous change in the boundary condition for the flow over the cavity between the fluid–solid and fluid–fluid interfaces. Subsequently, the numerically computed velocity was interpolated and integrated to yield the stream function. In figure 6, a comparison between analytical and numerical results is displayed for two different cases: (*a*) water flowing over an air-filled cavity, and (*b*) air flowing over a water-filled cavity. These examples span a wide range of possible viscosity ratios. In both cases, an excellent agreement between the analytical and the numerical results is found, even in close proximity to the interface.

At the interface itself, the assumptions made in §2 can be verified. The basic assumption was that the flow inside the cavity can be represented by a slip-length function $\gamma(x)$. Together with the viscosity ratio, $N\gamma(x)$ forms a net local slip length. A comparison between the analytically and numerically obtained values of the normalized slip-length function is shown in figure 7(*a,b*) for water flowing over an air-filled cavity and vice versa. The analytical distribution is described
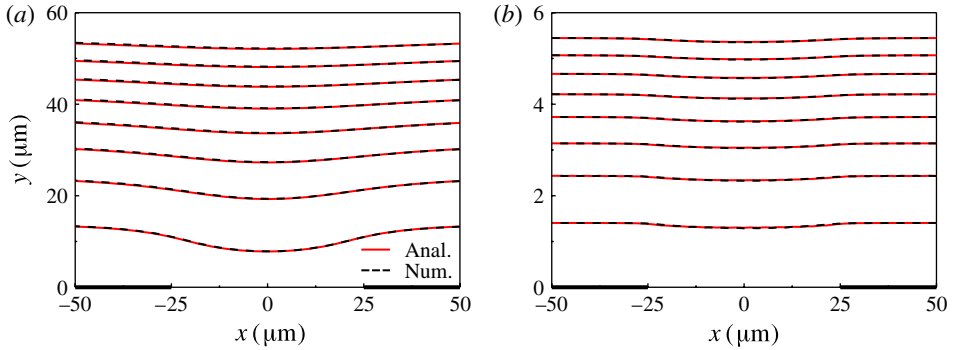
FIGURE 6. (Colour online) Comparison of the transverse flow streamlines calculated analytically with (3.21) and numerically: (*a*) water flowing over an air-filled cavity ($N \approx 55.56$); (*b*) air flowing over a water-filled cavity ($N \approx 0.02$). Note the different scales on the y axis in the two panels.

by (3.9) and (2.15), while the numerical local slip length explicitly obeys (2.3). The correspondence between the two curves is reasonable. Of course, the shape of the slip-length distribution does not coincide exactly, since the elliptic form was chosen due to mathematical rather than physical reasons. As mentioned before, it may be possible to calculate the flow field for slip-length distributions other than the elliptical one. However, in order to have a simple and viable model, it is not necessary to consider more complicated slip-length functions, since the integral of the local slip length agrees very well. This is important for the far-field behaviour of the solution, because the biharmonic equation (3.4) is of diffusive character. In other words, the biharmonic operator rapidly smears out local features of the flow field, which is then mainly determined by integral or averaged quantities a distance away from the boundaries. Nevertheless, figure 6 shows that the agreement between the assumed and the numerically determined slip-length distributions is good enough to give an accurate representation of the flow field even close to the cavity.

In the modelling, we took γ_t to be a function of the cavity aspect ratio alone, assuming its independence of the viscosity ratio N. Figure 7(*a,b*) show a slight dependence of γ_t on N in the numerical results. Still, taking into account the large span of viscosity ratios considered, this dependence is very weak. Furthermore, the integral local slip length remains unaffected.

Another important factor for the accuracy of the presented model is the order of magnitude of the maximum net local slip length $D_t N$. Despite having approximately the same deviations in the local slip-length distribution, the velocities at $y = 0$ of the analytical and numerical calculations agree very well in the case of water flowing over an air-filled cavity, i.e. at high N, while in the reversed case, i.e. at low N, the relation between the velocity curves resembles more that between the slip-length distributions (figure 7*c,d*). This fact is also apparent from the flow solution (3.23), where the term $4D_t N/(1 + 4D_t N)$ governs the behaviour of the equation. If the order of magnitude of $D_t N$ is large compared to unity, the flow field approaches the solution of Philip (1972), which, in fact, is of circular form. The elliptic ansatz is thus especially good at large $D_t N$. In a way, this can be understood as a natural generalization of the flow over a perfectly slipping interface. Hence, we conclude that the elliptic slip-length distribution
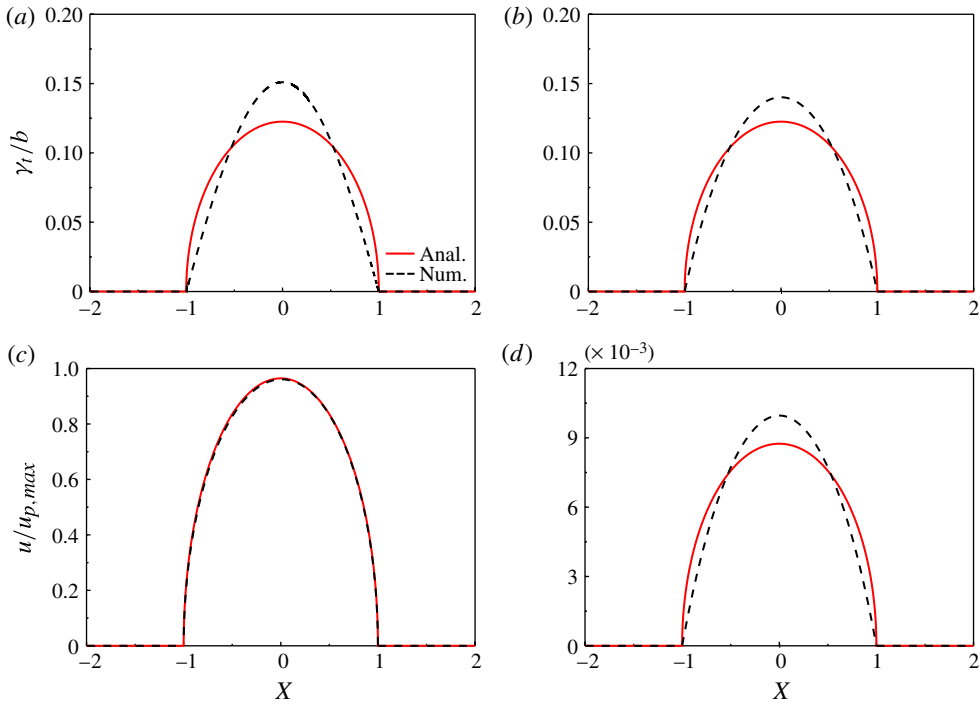
FIGURE 7. (Colour online) Comparison of the analytical and numerical results at $y = 0$. Normalized slip-length distribution (3.9) and (2.15): (*a*) water flowing over an air-filled cavity ($N \approx 55.56$); (*b*) air flowing over a water-filled cavity ($N \approx 0.02$). Normalized velocity from (3.21): (*c*) water on air; (*d*) air on water.

is a reasonable assumption, leading to a good agreement between analytical and numerical calculations over a large range of parameters.

In all calculations, the interface between the two fluids was assumed to be flat. The order of magnitude of the pressure exerted on the interface due to the shape of the streamlines will not exceed $\Delta p \sim \rho \left(u|_{x=0,y=0} \right)^2$. This pressure could possibly lead to a deformation of the interface creating a Laplace pressure of $\Delta p = \sigma/r$, with σ being the interfacial tension and r the radius of curvature. Hence, it will always depend on the specific combination of fluids investigated. However, assuming that the Reynolds number $Re < 1$ as above, the deflection of an air–water interface with $\sigma = 70$ mN m^{-1} and $b = 50$ μm is less than 2 nm, showing that in characteristic cases the flow field itself will not cause a significant interface deformation.

Flow over a cavity containing an immiscible fluid may occur in a variety of settings, for example, in aerodynamics, when capillary condensation takes place in a groove on a surface. Another special case is the flow over a superhydrophobic surface. It would be interesting to generalize (3.23) to a periodic array of cavities and subsequently to deduce an effective slip length for the entire surface. However, the calculation is not straightforward and cannot easily be performed with the mathematical methods employed in this paper. Therefore, we do not address such a calculation for now, and leave it for further investigation. Nevertheless, the flow over a single cavity is an important first step towards a description of the effective slip of a generalized superhydrophobic surface with an arbitrary fluid filling the cavities.

4. Longitudinal flow

We now address longitudinal shear flow over a cavity. The problem is mathematically closely related to the transverse flow problem. For an infinitely long cavity, the velocity w in the z direction is governed by the Laplace equation

$$\frac{\partial^2 w}{\partial x^2} + \frac{\partial^2 w}{\partial y^2} = 0. \tag{4.1}$$

The boundary conditions are equivalent to the transverse case, now applied to the velocity component w, i.e.

$$w = N\gamma_l(x)\frac{\partial w}{\partial y} \quad \text{for } |x| < \frac{b}{2}, \quad y = 0, \tag{4.2}$$

$$w = 0 \quad \text{for } |x| > \frac{b}{2}, \quad y = 0. \tag{4.3}$$

We can seek the solution to the above problem in terms of an analytic function $W_l(\mathfrak{z})$. The subscript l stands for the longitudinal flow direction. By definition, both the real and imaginary parts of $W_l(\mathfrak{z})$ fulfil the Laplace equation independently, hence we choose

$$w = \text{Im}(W_l(\mathfrak{z})). \tag{4.4}$$

This leads to the boundary conditions

$$\text{Im}(W_l) = N\gamma_l(x)\,\text{Re}(W_l') \quad \text{for } |x| < \frac{b}{2}, \quad y = 0, \tag{4.5}$$

$$\text{Im}(W_l) = 0 \quad \text{for } |x| > \frac{b}{2}, \quad y = 0, \tag{4.6}$$

and the condition for the stress at infinity,

$$\text{Re}(W_l') = \frac{\tau_\infty}{\eta_1} \quad \text{for } y \to \infty. \tag{4.7}$$

Obviously, the structure of this boundary value problem is identical to the transverse case (3.7) and (3.8). The function $W_l(\mathfrak{z})$ is directly related to $W_t(\mathfrak{z})$, since both are analytic and obey boundary conditions differing only by constant factors. Goursat's theorem can therefore also be understood as a relation between the transverse and the longitudinal flows.

Thus, the solution process for the longitudinal case follows exactly the procedure outlined above. This calculation (for intermediate steps see the Appendix) leads to a velocity

$$w = \frac{\tau_\infty}{\eta_1}\frac{1}{1 + 2D_lN}\left(y + 2D_lN\,\text{Im}\sqrt{(x + iy)^2 - \frac{1}{4}b^2}\right). \tag{4.8}$$

The velocity isolines corresponding to several viscosity ratios and the same cavity geometry as in the previous section are shown in figure 8. Analogously, $w_{p,max}$ is the maximum velocity at $y = 0$ for perfect slip. We observe the same flow-enhancing effect for large N as for the transverse case. Still, velocities are higher for the longitudinal flow, since $w_{p,max} = 2u_{p,max}$. This is in accordance with previous results (Philip 1972).
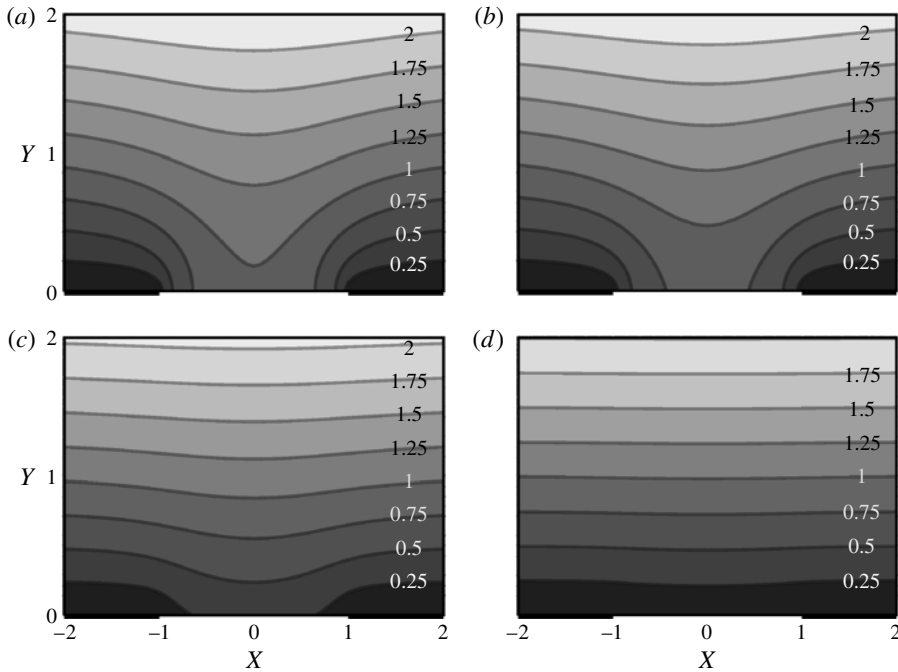
FIGURE 8. Longitudinal flow velocity $w/w_{p,max}$ for $D_l = 0.347$ and varying viscosity ratio: (*a*) $N = 100$; (*b*) $N = 10$; (*c*) $N = 1$; (*d*) $N = 0.1$.
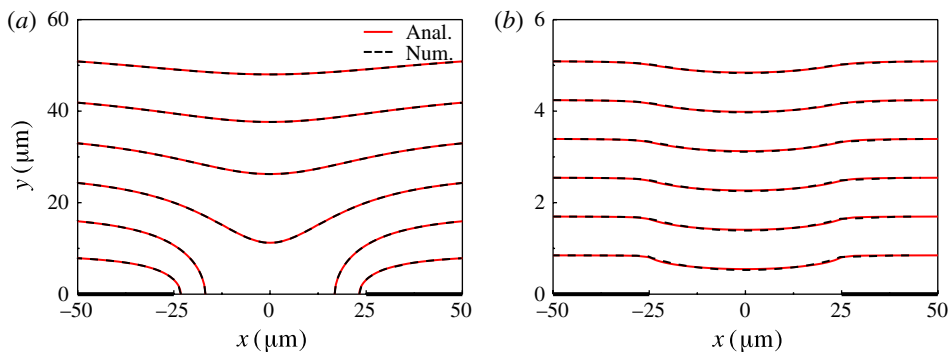

FIGURE 9. (Colour online) Comparison of the longitudinal velocity isolines calculated analytically with (4.8) and numerically: (*a*) water flowing over an air-filled cavity ($N \approx 55.56$); (*b*) air flowing over a water-filled cavity ($N \approx 0.02$). Note the different scales on the y axis in the two panels.

With D_l being described by (2.16), the agreement between analytical and numerical calculations is again excellent (figure 9). The behaviour of the solution at $y = 0$ is analogous to that of the transverse flow.

5. Conclusions

In this paper, we have investigated the flow over a rectangular cavity that contains a second immiscible fluid. Such a situation may arise in numerous practical applications, for example, in situations in which a gas flows along along a rough surface with

liquid-filled roughness features or when water flows along a superhydrophobic surface with entrapped gas bubbles.

In the calculation, the cavity is modelled as a boundary condition to the outer flow. The boundary condition appears in the form of a locally varying slip length, the functional form of which was determined by referring to previous results from lid-driven cavity flow. We derived the flow field complying with an elliptic slip-length distribution over the cavity. Together with a heuristic model for the magnitude of the local slip length, an analytical description of the flow over a cavity containing a second immiscible fluid is obtained. Up to now, analytical expressions for the flow field over such a cavity were known only for some limiting cases like a perfect viscosity-free fluid filling the cavity or an infinitely deep cavity. We have been able to formulate the problem in such a way that the flow over the cavity is directly related to the cavity geometry and the viscosity of the cavity fluid. We studied the flow in transverse and longitudinal directions. The two cases are connected via Goursat's theorem. The influence of the viscosity of the cavity medium on the outer flow was demonstrated. Naturally, the deviations from the flow field obtained for a solid wall are stronger for lower viscosity values. All results agree well with the known limiting cases. The analytical results have been compared to numerical calculations. The agreement between the two is extremely good.

Acknowledgements

Appendix

The mixed boundary value problem

$$\text{Im}(W_l) = N\gamma_l(x)\,\text{Re}(W_l') \quad \text{for } |x| < \frac{b}{2}, \quad y = 0, \tag{A 1}$$

$$\text{Im}(W_l) = 0 \quad \text{for } |x| > \frac{b}{2}, \quad y = 0, \tag{A 2}$$

$$\text{Re}(W_l') = \frac{\tau_\infty}{\eta_1} \quad \text{for } y \to \infty \tag{A 3}$$

is solved by the method of Sotkilava & Cherepanov (1974).

The auxiliary differential equation

$$F_l(\mathfrak{z}) = W_l'(\mathfrak{z}) - \frac{1}{2D_l N\sqrt{\mathfrak{z}^2 - \frac{1}{4}b^2}}\,W_l(\mathfrak{z}) \tag{A 4}$$

transforms the above problem to

$$\text{Re}(F_l(\mathfrak{z})) = 0 \quad \text{for } |x| < \frac{b}{2}, \quad y = 0, \tag{A 5}$$

$$\text{Im}(F_l(\mathfrak{z})) = 0 \quad \text{for } |x| > \frac{b}{2}, \quad y = 0, \tag{A 6}$$

$$\text{Re}(F_l(\mathfrak{z})) = \frac{\tau_\infty}{\eta_1}\left(1 - \frac{1}{2D_l N}\right) \quad \text{for } y \to \infty. \tag{A 7}$$

The solution for $F_l(\mathfrak{z})$ is given by the homogeneous part of the Keldysh–Sedov formula (3.15). Determining the coefficients according to the boundary conditions yields

$$F_l(\mathfrak{z}) = \frac{\tau_\infty}{\eta_1} \left(1 - \frac{1}{2D_l N} \right) \frac{\mathfrak{z}}{\sqrt{\mathfrak{z}^2 - \frac{1}{4}b^2}}. \tag{A 8}$$

Equation (A 4) can then be solved to give

$$W_l(\mathfrak{z}) = \frac{\tau_\infty}{\eta_1} \frac{\mathfrak{z} + 2D_l N \sqrt{\mathfrak{z}^2 - \frac{1}{4}b^2}}{1 + 2D_l N}. \tag{A 9}$$

REFERENCES

ATANACKOVIĆ, T. M. 1977 Slow viscous flows over a flat plate with mixed boundary conditions. *Ing.-Arch.* **46**, 157–160.

BELYAEV, A. V. & VINOGRADOVA, O. I. 2010 Effective slip in pressure-driven flow past super-hydrophobic stripes. *J. Fluid Mech.* **652**, 489–499.

BIBEN, T. & JOLY, L. 2008 Wetting on nanorough surfaces. *Phys. Rev. Lett.* **100**, 186103.

CHEREPANOV, G. P. 1977 *Mechanics of Brittle Fracture*. McGraw-Hill.

CICCOTTI, M., GEORGE, M., RANIERI, V., WONDRACZEK, L. & MARLIÈRE, C. 2008 Dynamic condensation of water at crack tips in fused silica glass. *J. Non-Cryst. Solids* **354**, 564–568.

COTTIN-BIZONNE, C., BARENTIN, C., CHARLAIX, É., BOCQUET, L. & BARRAT, J. L. 2004 Dynamics of simple liquids at heterogeneous surfaces: molecular-dynamics simulations and hydrodynamic description. *Eur. Phys. J.* E **15**, 427–438.

CROWDY, D. 2010 Slip length for longitudinal shear flow over a dilute periodic mattress of protruding bubbles. *Phys. Fluids* **22** (12), 121703.

DAVIS, A. M. J. & LAUGA, E. 2009 Geometric transition in friction for flow over a bubble mattress. *Phys. Fluids* **21** (1), 011701.

DAVIS, A. M. J. & LAUGA, E. 2010 Hydrodynamic friction of fakir-like superhydrophobic surfaces. *J. Fluid Mech.* **661**, 402–411.

FISHER, L. R., GAMBLE, R. A. & MIDDLEHURST, J. 1981 The Kelvin equation and the capillary condensation of water. *Nature* **290**, 575–576.

FISHER, L. R. & ISRAELACHVILI, J. N. 1979 Direct experimental verification of the Kelvin equation for capillary condensation. *Nature* **277**, 248–249.

GALLIERO, G. 2010 Lennard-Jones fluid–fluid interfaces under shear. *Phys. Rev.* E **81**, 056306.

GARABEDIAN, P. R. 1966 Free boundary flows of a viscous liquid. *Commun. Pure Appl. Maths.* **19** (4), 421–434.

HIGDON, J. J. L. 1985 Stokes flow in arbitrary two-dimensional domains: shear flow over ridges and cavities. *J. Fluid Mech.* **159**, 195–226.

HOCKING, L. M. 1976 A moving fluid interface on a rough surface. *J. Fluid Mech.* **76** (4), 801–817.

HU, Y., ZHANG, X. & WANG, W. 2010 Boundary conditions at the liquid–liquid interface in the presence of surfactants. *Langmuir* **26**, 10693–10702.

JOSEPH, D. D. & STURGES, L. 1978 The convergence of biorthogonal series for biharmonic and Stokes flow edge problems: Part II. *SIAM J. Appl. Maths.* **34** (1), 7–26.

JOVANOVIĆ, J., FROHNAPFEL, B. & DELGADO, A. 2010 Viscous drag reduction with surface-embedded grooves. In *Turbulence and Interactions* (ed. M. O. Deville, T.-H. Lê & P. Sagaut), *Notes on Numerical Fluid Mechanics and Multidisciplinary Design*, vol. 110, pp. 191–197. Springer.

KARNIADAKIS, G., BESKOK, A. & ALURU, N. 2005 *Microflows and Nanoflows*. Springer.

KELDYSH, M. & SEDOV, L. 1937 Sur la solution effective de quelques problèmes limites pour les fonctions harmoniques. *Dokl. Acad. Nauk USSR* **16** (1), 7–10.

LAUGA, E., BRENNER, M. P. & STONE, H. A. 2005 Microfluidics: the no-slip boundary condition. In *Handbook of Experimental Fluid Dynamics* (ed. J. Foss, C. Tropea & A. Yarin). Springer.

LAUGA, E. & STONE, H. A. 2003 Effective slip in pressure-driven Stokes flow. *J. Fluid Mech.* **489**, 55–77.

LAWRENTJEW, M. A. & SCHABAT, B. W. 1967 *Methoden der komplexen Funktionentheorie*. VEB Deutscher.

LEE, C., CHOI, C.-H. & KIM, C.-J. 2008 Structured surfaces for a giant liquid slip. *Phys. Rev. Lett.* **101**, 064501.

MA, M. & HILL, R. M. 2006 Superhydrophobic surfaces. *Curr. Opin. Colloid Interface Sci.* **11** (4), 193–202.

MOFFATT, H. K. 1963 Viscous and resistive eddies near a sharp corner. *J. Fluid Mech.* **18** (1), 1–18.

MUSKHELISHVILI, N. I. 1975 *Some Basic Problems of the Mathematical Theory of Elasticity*. Noordhoff International.

MUSKHELISHVILI, N. I. 2008 *Singular Integral Equations*. Dover.

NAVIER, M. 1823 Mémoire sur les lois du mouvement des fluides. *Mém. Acad. R. Sci. Inst. Fr.* **6**, 389–440.

NOSONOVSKY, M. & BHUSHAN, B. 2008 Roughness-induced superhydrophobicity: a way to design non-adhesive surfaces. *J. Phys.: Condens. Matter* **20** (22), 225009.

PAN, F. & ACRIVOS, A. 1967 Steady flows in rectangular cavities. *J. Fluid Mech.* **28** (4), 643–655.

PHILIP, J. R. 1972 Flows satisfying mixed no-slip and no-shear conditions. *Z. Angew. Math. Phys.* **23** (3), 353–372.

PRASAD, A. K. & KOSEFF, J. R. 1989 Reynolds number and end-wall effects on a lid-driven cavity flow. *Phys. Fluids* A **1** (2), 208–218.

ROTHSTEIN, J. P. 2010 Slip on superhydrophobic surfaces. *Annu. Rev. Fluid Mech.* **42** (1), 89–109.

SBRAGAGLIA, M. & PROSPERETTI, A. 2007 A note on the effective slip properties for microchannel flows with ultrahydrophobic surfaces. *Phys. Fluids* **19**, 043603.

SHANKAR, P. N. 1993 The eddy structure in Stokes flow in a cavity. *J. Fluid Mech.* **250**, 371–383.

SHANKAR, P. N. & DESHPANDE, M. D. 2000 Fluid mechanics in the driven cavity. *Annu. Rev. Fluid Mech.* **32** (1), 93–136.

SHEN, C. & FLORYAN, J. M. 1985 Low Reynolds number flow over cavities. *Phys. Fluids* **28** (11), 3191–3202.

SMIRNOW, W. I. 1974 *Lehrgang der höheren Mathematik, III*, vol. 4. VEB Deutscher.

SOTKILAVA, O. V. & CHEREPANOV, C. P. 1974 Some problems of the nonhomogeneous elasticity theory. *Prikl. Mat. Mekh.* **38** (3), 539–550.

STEINBERGER, A., COTTIN-BIZONNE, C., KLEIMANN, P. & CHARLAIX, E. 2007 High friction on a bubble mattress. *Nat. Mater.* **6**, 665–668.

TSAI, P., PETERS, A. M., PIRAT, C., WESSLING, M., LAMMERTINK, R. G. H. & LOHSE, D. 2009 Quantifying effective slip length over micropatterned hydrophobic surfaces. *Phys. Fluids* **21** (11), 112002.

VISWANATH, P. R. 2002 Aircraft viscous drag reduction using riblets. *Prog. Aerosp. Sci.* **38**, 571–600.

YANG, S., DAMMER, S. M., BREMOND, N., ZANDVLIET, H. J. W., KOOIJ, E. S. & LOHSE, D. 2007 Characterization of nanobubbles on hydrophobic surfaces in water. *Langmuir* **23** (13), 7072–7077.

YBERT, C., BARENTIN, C., COTTIN-BIZONNE, C., JOSEPH, P. & BOCQUET, L. 2007 Achieving large slip with superhydrophobic surfaces: scaling laws for generic geometries. *Phys. Fluids* **19** (12), 123601.